arXiv:2208.05306v1 [math.NA] 10 Aug 2022

AN EXPLICIT TOTAL LAGRANGIAN FRAGILE POINTS METHOD FOR FINITE DEFORMATION OF HYPERELASTIC MATERIALS

A PREPRINT

Konstantinos A. Mountris*
Mechanical Engineering
University College London
London, United Kingdom
k.mountris@ucl.ac.uk

Mingjing Li
School of Aeronautic Science & Engineering
Beihang University
Beijing, China
10756@buaa.edu.cn

Richard Schilling
Barts Heart Centre
St Bartholomew's Hospital
London, United Kingdom
richard.schilling@nhs.net

Leiting Dong
School of Aeronautic Science & Engineering
Beihang University
Beijing, China
ltdong@buaa.edu.cn

Satya N. Atluri
Mechanical Engineering
Texas Tech University
Lubbock, Texas
snatluri.ttu@gmail.com

Alicia Casals
Automatic Control & Computer Engineering
Universitat Politecnica de Catalunya
Barcelona, Spain
alicia.casals@upc.edu

Helge A. Wurdemann
Mechanical Engineering
University College London
London, United Kingdom
h.wurdemann@ucl.ac.uk

August 11, 2022

ABSTRACT

This research explored a novel explicit total Lagrangian Fragile Points Method (FPM) for finite deformation of hyperelastic materials. In contrast to mesh-based methods, where mesh distortion may pose numerical challenges, meshless methods are more suitable for large deformation modelling since they use enriched shape functions for the approximation of displacements. However, this comes at the expense of extra computational overhead and higher-order quadrature is required to obtain accurate results. In this work, the novel meshless method FPM was used to derive an explicit total Lagrangian algorithm for finite deformation. FPM uses simple one-point integration for exact integration of the Galerkin weak form since it employs simple discontinuous polynomials as trial and test functions, leading to accurate results even with single-point quadrature. The proposed method was evaluated by comparing it with FEM in several case studies considering both the extension and compression of a hyperelastic material. It was demonstrated that FPM maintained good accuracy even for large deformations where FEM failed to converge.

Keywords total Lagrangian · explicit time integration · Fragile Points Method · hyperelasticity · large deformation

1 Introduction

Rubber-like materials such as elastomers and soft tissue are commonly modelled under the assumption of a hyperelastic constitutive model where the stress–strain relationship is derived from a strain energy density function [1]. The Finite Element Method (FEM) is frequently used to simulate the elastic response of these materials when they undergo a large deformation. Although FEM is the standard numerical method for finite deformation analysis, it suffers from

*[mail] k.mountris@ucl.ac.uk [url] https://www.mountris.org

low convergence in conditions of large deformation and near-incompressibility [2]. Even when non-locking elements are utilised, convergence and overall accuracy are significantly deteriorated [3] due to the large mesh distortion. A remedy to the mesh distortion problem is to remesh the deformed geometry during the evolution of the deformation [4]. However, this solution is not time efficient, especially for soft tissue simulation where results should be generated by taking into account the time restrictions of the corresponding clinical application.

Over the past several decades, meshless methods have been developed and demonstrated as being more suitable for finite deformation compared to FEM. Meshless methods either partially or fully alleviate the mesh requirement, avoiding the FEM mesh distortion problem. Examples of meshless methods include the smoothed particle hydrodynamics (SPH) [5, 6], the meshless local Petrov-Galerkin (MLPG) [7, 8], and the element free Galerkin (EFG) methods [9, 10]. The SPH method has been used successfully to derive a total Lagrangian formulation of SPH for large deformation simulation in 3D cardiac mechanics [11]. Since gradients of constant and linear functions are not correctly obtained in the standard SPH method, a corrected smoothed particle method [12] was used to ensure the conservation of linear and angular momentum. The MLPG is another method that has been proposed as an alternative to FEM for large deformation simulations [2, 8]. Enriched radial basis functions with a polynomial basis function were used for constructing the MLPG trial functions. The polynomial basis function enrichment allowed the exact imposition of essential boundary conditions. Large deformation was simulated in a series of 2D benchmark problems demonstrating superior accuracy for MLPG compared to FEM.

In a similar manner to SPH and MLPG, the EFG method has been employed for solving large deformation problems. An EFG-based algorithm, the so-called Meshless Total Lagrangian Explicit Dynamics (MTLED) algorithm, has been used to a great extent for the simulation of large deformations in biomechanics [13, 14]. The MTLED employs the EFG method to solve the total Lagrangian formulation explicitly using a central difference scheme. Initially, the method was introduced using the Moving Least Squares (MLS) for the approximation of trial functions [15]. It is well known that MLS do not possess the Kronecker delta property, and therefore the essential boundary conditions cannot be imposed directly as in FEM. An efficient algorithm for the imposition of the exact essential boundary conditions in MTLED has been introduced in [13]. However, the application of such treatments for the imposition of essential boundary conditions can be avoided by replacing the MLS approximation functions. In [16], the Cell-based Maximum Entropy (CME) approximants have been proposed as an alternative to MLS. CME possesses the weak Kronecker delta property that allows applying essential boundary conditions directly and exactly as in FEM. An alternative approach is followed in [17], where a regularized weight function [18] is used for the construction of MLS, rendering the approximation almost interpolating. Both approaches presented accurate imposition of essential boundary conditions in several 3D benchmark problems and were cross-validated against analytical solutions and FEM [16, 17].

The aforementioned meshless methods are valuable alternatives to FEM for large deformation simulations. However, they possess drawbacks, including the requirement for complex algorithms to impose the essential boundary conditions and inexact integration due to the complexity of the approximation functions that lead to the requirement of high–order integration to improve accuracy [19]. Therefore, although meshless methods can reduce dramatically the preprocessing time, their computational cost is usually significantly higher than FEM [20]. Recently, a novel Fragile Points Method (FPM) that inherently avoids these limitations has been introduced by the groups of Atluri and Dong [21, 22]. In FPM, the problem domain Ω is discretized by distributing points randomly in its interior and boundary. Following this step, Ω is partitioned in contiguous and non-overlapping subdomains that involve a single node, usually at the centroid of the subdomain. The meshless approximation is then constructed on a compact support domain that includes the points for which their subdomain shares an interface with the subdomain of the point of interest. Trial and test functions which are local, simple, polynomial, and discontinuous are employed as [23]. Therefore, integration becomes trivial and low-order integration is sufficient to compute integrals with high accuracy in contrast to previous meshless methods. Moreover, both essential and natural boundary conditions are imposed directly as in FEM without the need for additional treatment. Nevertheless, it should be noted that deriving the standard Galerkin weak form with the FPM will lead to inconsistent and inaccurate solutions due to the discontinuity of the employed trial and test functions. To remedy this issue, interior penalty numerical flux corrections, which are commonly used in Discontinuous Galerkin methods [24], are employed to restore the consistency and accuracy of the FPM-derived Galerkin weak form.

Despite its recent introduction, FPM has successfully simulated different problems and provided results in agreement with FEM while reducing the requirement for a high-quality mesh. In addition, FPM was validated by solving the patch test and the Poisson equation in 1D and 2D then comparing its convergence to FEM [21]. FPM demonstrated higher accuracy than FEM when mesh quality was deteriorated due to mesh distortion. Moreover, FPM has been successful in solving 2D linear elasticity [22] and heat conduction [25] problems in 2D and 3D. Furthermore, it has been demonstrated as a promising alternative to FEM for cardiac modelling applications. Results with similar accuracy to FEM were obtained for cardiac electrophysiology simulation through the monodomain reaction-diffusion model [26]. Similarly, high correlation of FPM with FEM was obtained when solved the Laplace-Dirichlet problem for the determination of cardiac muscle fiber orientation by [27]. Finally, FPM possesses the ability to model crack develop-

ments in a very simple manner due to the discontinuity of the trial and test functions. It has been used successfully for modelling flexoelectric problems with crack propagation [28] and damage as well as fracture of U-notched structures [29].

In this work, we hypothesize that FPM is a promising alternative to FEM for finite deformation simulation, especially when large mesh distortion occurs during deformation. Therefore, FPM is employed to derive the total Lagrangian formulation to simulate the large deformation of hyperelastic materials using explicit integration in time as in MTLED [15, 14]. Since FPM allows for direct imposition of essential and natural boundary conditions as well as accurate approximation of integrals with low-order integration rules, accurate and efficient solutions to large deformation problems are expected. The structure of the remaining paper is as follows. In section 2, the FPM total Lagrangian formulation is described, with details provided about the derivation of the explicit total Lagrangian algorithm, the formulation of the FPM trial and test functions, and the application of the interior penalty numerical flux correction. In section 3, the FPM total Lagrangian algorithm is evaluated in a series of validation case studies and the obtained solutions are compared with FEM simulations. Finally, a discussion about the findings of this work and a conclusion with future work directions are provided in sections 4 and 5, respectively.

2 Explicit Total Lagrangian Fragile Points Method

2.1 Problem definition

Consider the boundary value problem of an elastomer undergoing large deformation and governed by the following equations expressed in the reference configuration (total Lagrangian formulation) [30]:

$$\begin{aligned} \nabla_0 \boldsymbol{P} + \rho_0 \boldsymbol{b} &= \rho_0 \ddot{\boldsymbol{u}} \quad \text{in } \Omega_0 \\ \boldsymbol{u} &= \bar{\boldsymbol{u}} \quad \text{in } \Gamma_u \\ \boldsymbol{P} \cdot \boldsymbol{n}_0 &= \bar{\boldsymbol{t}} \quad \text{in } \Gamma_t \end{aligned} \tag{1}$$

In Equation (1), $\boldsymbol{P}$ denotes the first Piola-Kirchhoff stress tensor, $\rho_0 \boldsymbol{b}$ the body forces per unit reference volume, $\ddot{\boldsymbol{u}}$ the second time derivative of the displacement, and $\boldsymbol{n}_0$ the outward unit surface normal. The subscript 0 delineates field values expressed in respect with the reference configuration. Therefore, Ω_0 is the region occupied by the body in its reference configuration while Γ_u and Γ_t are the parts of the boundary $\Gamma = \Gamma_u \bigcup \Gamma_t$ where boundary conditions are imposed on displacement and traction, respectively. The weak form of Equation (1) is obtained by replacing $\boldsymbol{u}$ with a trial function $\boldsymbol{u}^h$ and minimizing the resulting residual through multiplication by the test function $\boldsymbol{v}$ and integration to obtain:

$$\int_{\Omega_0} \nabla_0 \boldsymbol{P}(\boldsymbol{u}^h) \cdot \boldsymbol{v} d\Omega + \int_{\Omega_0} \rho_0 (\boldsymbol{b} - \ddot{\boldsymbol{u}}^h) \cdot \boldsymbol{v} d\Omega = 0 \tag{2}$$

Applying the divergence theorem and the traction boundary condition, the weak form can be rewritten as:

$$\int_{\Omega_0} \boldsymbol{S} : \boldsymbol{E} d\Omega - \int_{\Omega_0} \rho_0 (\boldsymbol{b} - \ddot{\boldsymbol{u}}^h) \cdot \boldsymbol{v} d\Omega - \int_{\Gamma_t} \bar{\boldsymbol{t}} \cdot \boldsymbol{v} d\Gamma = 0 \tag{3}$$

where the first Piola-Kirchhoff stress tensor is replaced by the second Piola-Kirchhoff stress tensor ($\boldsymbol{S}$) through $\boldsymbol{P} = \boldsymbol{S}\boldsymbol{F}$ and $\boldsymbol{E}$ denotes the Green-Lagrange strain tensor obtained via $\boldsymbol{E} = \frac{1}{2}\left[\nabla \boldsymbol{v}^T \boldsymbol{F} + \boldsymbol{F}^T \nabla \boldsymbol{v}\right]$ with $\boldsymbol{F}$ being the deformation gradient tensor. $\boldsymbol{S}$ is obtained by differentiating the material's strain energy density (W) by $\boldsymbol{E}$:

$$\boldsymbol{S} = \frac{\partial W}{\partial \boldsymbol{E}} = \frac{\partial W}{\partial J_1}\frac{\partial J_1}{\partial \boldsymbol{E}} + \frac{\partial W}{\partial J_2}\frac{\partial J_2}{\partial \boldsymbol{E}} + \frac{\partial W}{\partial J_3}\frac{\partial J_3}{\partial \boldsymbol{E}} \tag{4}$$

where J_1, J_2, J_3 denote the reduced invariants of the right Cauchy-Green deformation tensor. In FPM, the reference configuration domain (Ω_0) is discretized by a number of randomly distributed points inside the domain and on its boundary. The domain is then further partitioned into contiguous and non-overlapping subdomains of arbitrary shapes as shown in Figure 1. Using the same type of trial function $\boldsymbol{u}^h$ and test function $\boldsymbol{v}$ in each subdomain, the discretized Galerkin weak form is obtained:

$$\sum_{E \in \Omega_0} \int_E \boldsymbol{S} : \boldsymbol{E} d\Omega - \sum_{E \in \Omega_0} \int_E \rho_0 (\boldsymbol{b} - \ddot{\boldsymbol{u}}^h) \cdot \boldsymbol{v} d\Omega - \sum_{e \in \Gamma_t} \int_e \bar{\boldsymbol{t}} \cdot \boldsymbol{v} d\Gamma = 0 \tag{5}$$

where $\int_E$ denotes integration over the subdomain $E \in \Omega_0$, and $\int_e$ denotes integration over the subdomain's boundary $e \in \Gamma_t$, which belongs to the traction boundary.

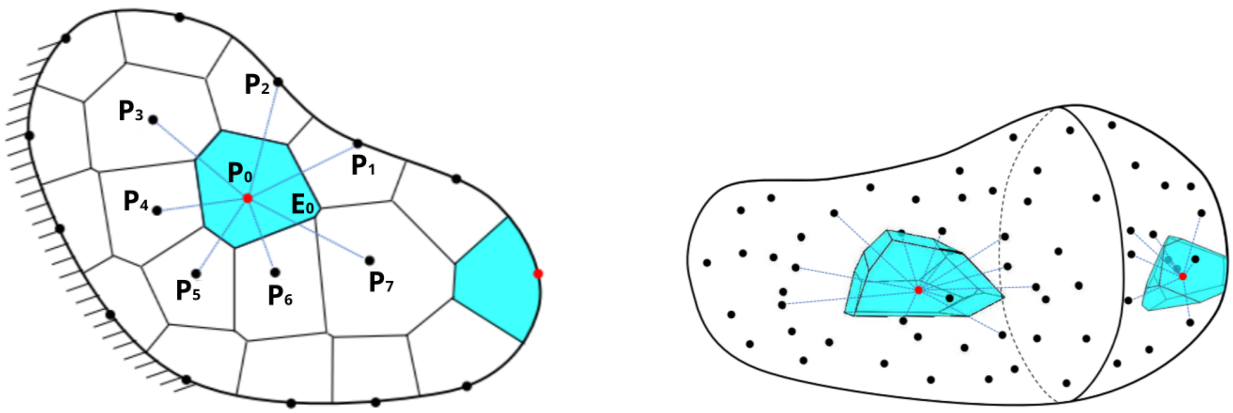

(a) (b)

Figure 1: Partitioning of domain Ω_0. (a) 2D domain partitioning with points distributed inside it and on its boundary ($P \in \Omega_0 \bigcup \Gamma$). (b) 3D domain partitioning with points distributed inside it ($P \in \Omega_0$).

2.2 Derivation of FPM trial and test functions

In each subdomain, trial and test functions are constructed by defining local discontinuous polynomial displacement vectors $\boldsymbol{u}^h$ and $\boldsymbol{v}$. Following the formulation in [22] and assuming that Ω_0 is defined in $\mathbb{R}^2$, the trial function $\boldsymbol{u}^h \equiv \boldsymbol{u}^h(x, y)$ on the subdomain E_0, which encloses the point P_0, can be obtained by:

$$\boldsymbol{u}^h(x,y) = \begin{bmatrix} u_x^h \\ u_y^h \end{bmatrix} = \begin{bmatrix} u_x^0 + \left.\frac{\partial u_x}{\partial x}\right|_{P_0}(x - x_0) + \left.\frac{\partial u_x}{\partial y}\right|_{P_0}(y - y_0) \\ u_y^0 + \left.\frac{\partial u_y}{\partial x}\right|_{P_0}(x - x_0) + \left.\frac{\partial u_y}{\partial y}\right|_{P_0}(y - y_0) \end{bmatrix} (x,y) \in E_0 \tag{6}$$

where (x_0, y_0) denote the coordinates of P_0, $[u_x^0 \quad u_y^0]^T$, the value of $\boldsymbol{u}^h$ at P_0, and $\left.\begin{bmatrix} \frac{\partial u_x}{\partial x} & \frac{\partial u_x}{\partial y} & \frac{\partial u_y}{\partial x} & \frac{\partial u_y}{\partial y} \end{bmatrix}^T\right|_{P_0}$, the unknown derivatives of which are computed using the generalized Finite Difference Method [23]. The support domain for P_0 is defined as the group of points $P_1, P_2, \ldots, P_m$ that are involved in the subdomains $E_1, E_2, \ldots, E_m$, which share an interface with subdomain E_0 (see Figure 1). We define the weighted discrete L^2 norm ($\boldsymbol{J}$) given in matrix form by:

$$\boldsymbol{J} = (\boldsymbol{A}\boldsymbol{\alpha} + \boldsymbol{u}_0 - \boldsymbol{u}_m)^T \boldsymbol{W} (\boldsymbol{A}\boldsymbol{\alpha} + \boldsymbol{u}_0 - \boldsymbol{u}_m) \tag{7}$$

where

$$\boldsymbol{A} = \begin{bmatrix} x_1 - x_0 & y_1 - y_0 & 0 & 0 \\ 0 & 0 & x_1 - x_0 & y_1 - y_0 \\ x_2 - x_0 & y_2 - y_0 & 0 & 0 \\ 0 & 0 & x_2 - x_0 & y_2 - y_0 \\ \vdots & \vdots & \vdots & \vdots \\ x_m - x_0 & y_m - y_0 & 0 & 0 \\ 0 & 0 & x_m - x_0 & y_m - y_0 \end{bmatrix}$$

$$\boldsymbol{a} = \left.\begin{bmatrix} \frac{\partial u_x}{\partial x} & \frac{\partial u_x}{\partial y} & \frac{\partial u_y}{\partial x} & \frac{\partial u_y}{\partial y} \end{bmatrix}^T\right|_{P_0}$$

$$\boldsymbol{u}_0 = \begin{bmatrix} u_x^0 & u_y^0 & u_x^0 & u_y^0 & \ldots & u_x^0 & u_y^0 \end{bmatrix}^T_{1\times 2m}$$

$$\boldsymbol{u}_m = \begin{bmatrix} u_x^1 & u_y^1 & u_x^2 & u_y^2 & \ldots & u_x^m & u_y^m \end{bmatrix}^T$$

$$\boldsymbol{W} = \begin{bmatrix} w_x^1 & 0 & 0 & \dots & 0 \\ 0 & w_y^1 & \ddots & \ddots & \vdots \\ 0 & \ddots & \ddots & \ddots & 0 \\ \vdots & \ddots & \ddots & w_x^m & 0 \\ 0 & \dots & 0 & 0 & w_y^m \end{bmatrix}$$

In the above matrices, (x_i, y_i) denote the coordinates of point P_i, $\begin{bmatrix} u_x^i & u_y^i \end{bmatrix}^T$ and the value of $\boldsymbol{u}^h$ at P_i, $\begin{bmatrix} w_x^i & w_y^i \end{bmatrix}^T$ is the value of the weight function at P_i, $i = 1, 2, \dots, m$. The derivatives vector $\boldsymbol{a}$ is derived by solving the stationarity of $\boldsymbol{J}$ (Equation 7) to obtain:

$$\boldsymbol{a} = (\boldsymbol{A}^T \boldsymbol{W} \boldsymbol{A})^{-1} \boldsymbol{A}^T \boldsymbol{W} (\boldsymbol{u}^m - \boldsymbol{u}^0) \tag{8}$$

By expressing $\boldsymbol{u}^m - \boldsymbol{u}^0$ as:

$$\boldsymbol{u}^m - \boldsymbol{u}^0 = [\boldsymbol{I}_1 \quad \boldsymbol{I}_2] \boldsymbol{u}_E \tag{9}$$

where

$$\boldsymbol{u}_E = \begin{bmatrix} u_x^0 & u_y^0 & u_x^1 & u_y^1 & \dots & u_x^m & u_y^m \end{bmatrix}^T$$

$$\boldsymbol{I}_1 = \begin{bmatrix} -1 & 0 \\ 0 & -1 \\ -1 & 0 \\ 0 & -1 \\ \vdots & \vdots \\ -1 & 0 \\ 0 & -1 \end{bmatrix}_{2m \times 2} \qquad \boldsymbol{I}_2 = \begin{bmatrix} 1 & 0 & \dots & 0 \\ 0 & 1 & \ddots & \vdots \\ \vdots & \vdots & \ddots & 0 \\ 0 & \dots & 0 & 1 \end{bmatrix}_{2m \times 2m} \tag{10}$$

we can rewrite vector $\boldsymbol{a}$ as:

$$\boldsymbol{a} = \boldsymbol{C} \boldsymbol{u}_E \tag{11}$$

where

$$\boldsymbol{C} = (\boldsymbol{A}^T \boldsymbol{W} \boldsymbol{A})^{-1} \boldsymbol{A}^T \boldsymbol{W} [\boldsymbol{I}_1 \quad \boldsymbol{I}_2] \tag{12}$$

Finally, by substituting Equation (12) in Equation (6), we obtain:

$$\boldsymbol{u}^h = \boldsymbol{N} \boldsymbol{u}_E \tag{13}$$

where the matrix $\boldsymbol{N}$ is the shape function of $\boldsymbol{u}^h$ in E_0 and is given by:

$$\begin{aligned} \boldsymbol{N} &= \begin{bmatrix} x - x_0 & y - y_0 & 0 & 0 \\ 0 & 0 & x - x_0 & y - y_0 \end{bmatrix} \boldsymbol{C} + \boldsymbol{I}_3 \\ \boldsymbol{I}_3 &= \begin{bmatrix} 1 & 0 & 0 & \dots & 0 \\ 0 & 1 & 0 & \dots & 0 \end{bmatrix}_{2 \times (2m+2)} \end{aligned} \tag{14}$$

Since the presented FPM is based on the Galerkin weak form, the test function v is derived in a similar manner to the trial function u_h. As there are no continuity requirements at the interfaces of the subdomains, the trial and test functions are discontinuous point-based simple and local polynomials. Due to the discontinuity, the Galerkin weak form leads to inconsistent and inaccurate solutions if continuity is not restored. It should be noted that instead of deriving the unknown derivatives by using the generalized Finite Difference Method, one may also employ the Differential Quadrature Method as was used in [28].

2.3 Interior penalty numerical flux correction

To solve the inconsistency problem, an interior penalty numerical flux correction is introduced, which is similar to discontinuous Galerkin FEM. The interior penalty numerical flux correction is commonly used in discontinuous Galerkin FEM to retrieve the continuity at the element interfaces [24]. Similarly, consistency and accuracy in FPM are ensured by applying the interior penalty numerical flux correction to modify the Galerkin weak form in Equation (5). This treatment can be viewed as applying a corrective internal force which acts on the interior interface $e \in \Gamma_h$ of subdomain E and its neighbour, where Γ_h denotes the interior part of Γ. Therefore, Equation (5) is modified as:

$$\sum_{E \in \Omega_0} \int_E \boldsymbol{S} : \delta \boldsymbol{E} d\Omega - \sum_{E \in \Omega_0} \int_E \rho_0 (\boldsymbol{b} - \ddot{\boldsymbol{u}}^h) \cdot \boldsymbol{v} d\Omega - \sum_{e \in \Gamma_t} \int_e \bar{\boldsymbol{t}} \cdot \boldsymbol{v} d\Gamma - \sum_{e \in \Gamma_h} \int_e \boldsymbol{t}^* \cdot [\![\boldsymbol{v}]\!] d\Gamma = 0 \tag{15}$$

The numerical flux correction is defined using the incomplete interior penalty Galerkin (IIPG) method as in [29], which has an explicit physical meaning as the traction acting on the interior interface. The interior interface traction $\boldsymbol{t}^*$ is obtained by:

$$\begin{aligned} \boldsymbol{t}^* &= \{\, \boldsymbol{t}_h \} - \boldsymbol{\beta}[\![\boldsymbol{u}]\!] \\ \boldsymbol{t}_h &= \frac{1}{2}\left(\boldsymbol{P}^+\boldsymbol{n}_0^+ + \boldsymbol{P}^-\boldsymbol{n}_0^-\right) - \boldsymbol{\beta}[\![\boldsymbol{u}]\!] \end{aligned} \tag{16}$$

where $[\![\ ]\!]$ and $\{\ \}$ are the jump and average operators, respectively. For any interior interface $e \in \partial E^+ \bigcap \partial E^-$ shared by the neighbouring subdomains E^+ and E^-, the operators act on an arbitrary quantity w as:

$$[\![w]\!] = w|_e^{E^+} - w|_e^{E^-}, \quad \{w\} = \frac{1}{2}\left(w|_e^{E^+} + w|_e^{E^-}\right) \tag{17}$$

In Equation (16), $\boldsymbol{\beta}$ is a second-order penalty tensor used to weakly enforce displacement continuity across the interior interfaces. It is defined as a diagonal matrix:

$$\boldsymbol{\beta} = \frac{pE}{h_s}\boldsymbol{I} \tag{18}$$

where p denotes a penalty coefficient, E the Young's modulus, and h_s the subodmain characteristic length. $\boldsymbol{P}^+$, $\boldsymbol{P}^-$ denote the first Piola-Kirchhoff stress tensors for the two neighboring subdomains, while $\boldsymbol{n}_0^+$, $\boldsymbol{n}_0^-$ are the outward normal vectors to the interface of the neighboring subdomains at the reference configuration. The penalty tensor $\boldsymbol{\beta}$ is viewed as the interfacial stiffness. Therefore, the term $\boldsymbol{\beta}[\![\boldsymbol{u}]\!]$ in Equation (16) controls the contribution of separation between the neighboring subdomains, and $\boldsymbol{t}^*$ can be viewed as the exact traction acting on each interior interface, considering both the stress in the subdomains and the separation across the internal interface.

2.4 Explicit integration in time

The consistent Galerkin weak form in Equation (15) can be written in matrix form as:

$$\boldsymbol{M}\ddot{\boldsymbol{u}} + \boldsymbol{F}^{\boldsymbol{int}} = \boldsymbol{F}^{\boldsymbol{ext}} \tag{19}$$

where $\boldsymbol{u}$ denotes the displacements vector, $\boldsymbol{M}$ the mass matrix, $\boldsymbol{F}^{\boldsymbol{int}}$ the internal forces, and $\boldsymbol{F}^{\boldsymbol{ext}}$ the external forces (including body and traction forces). Applying mass lumping to diagonalize $\boldsymbol{M}$ allows solving Equation (19) explicitly using the central difference time integration scheme. Therefore, at each integration time step k, we obtain:

$$\boldsymbol{u}_{k+1} = \boldsymbol{u}_k + dt_{k+1}\dot{\boldsymbol{u}}_k + \frac{1}{2dt_{k+1}^2}\ddot{\boldsymbol{u}}_k, \tag{20}$$

$$\dot{\boldsymbol{u}}_{k+1} = \dot{\boldsymbol{u}}_k + \frac{1}{2dt_{k+1}^2}(\ddot{\boldsymbol{u}}_{k+1} + \ddot{\boldsymbol{u}}_k), \tag{21}$$

$$\boldsymbol{F}^{\boldsymbol{int}} = \sum_{E\in\Omega}\boldsymbol{F}_k^E - \sum_{e\in\Gamma_h}\tilde{\boldsymbol{F}}_k^e = \sum_{E\in\Omega}\int_E \boldsymbol{B}^T\boldsymbol{S}_k d\Omega - \sum_{e\in\Gamma_h}\int_e [\![\boldsymbol{N}]\!]^T\boldsymbol{t}_k^* d\Gamma, \tag{22}$$

$$\frac{1}{dt^2}\boldsymbol{M}\boldsymbol{u}_{k+1} = \boldsymbol{R}_k - \sum_{E\in\Omega}\boldsymbol{F}_k^E - \frac{1}{dt^2}\boldsymbol{M}(\boldsymbol{u}_{k-1} - 2\boldsymbol{u}_k) \tag{23}$$

where $\boldsymbol{B}_k$ is the strain–displacement matrix at step k. It should be noted that there is no need to assemble the stiffness matrix $\boldsymbol{K}$ as Equations (20)–(23) are solved explicitly. Internal forces are computed at the level of the non-overlapping subdomains. However, since explicit methods are only conditionally stable, an adequately small integration time step dt must be selected to ensure the stability of the solution. An estimation of the critical stable time step is derived as in [31]:

$$\bar{d}t_{crit} = min_j\left(\frac{2}{\sqrt{\lambda_j^{max}}}\right) \tag{24}$$

where λ_j^{max} is the maximum eigenvalue of the stiffness matrix. The upper bound at a node j enclosed by subdomain E_j is calculated by:

$$\lambda_j^{max} \leq m_j c^2 \boldsymbol{C}\boldsymbol{C}^T \tag{25}$$

where m_j is the number of neighbouring points in the support domain of point j and $c^2 = \frac{\lambda+2\mu}{\rho_0}$ is the dilatation wave speed squared with λ. In this instance, λ, μ are the Lamé parameters and $\boldsymbol{C}$ the matrix of the FPM derivatives as given in Equation (12). It should be noted that the numerical flux correction term affects the numerical high-frequency

eigenmodes [32]. Therefore, the critical time step stability criterion must be modified. As described in [32], reducing the critical stable time step by the square root of the penalty coefficient is required. Therefore, Equation (24) should be updated to:

$$dt_{crit} = \frac{1}{\sqrt{p}} \bar{dt}_{crit}, \quad p > 0 \tag{26}$$

3 Validation case studies

In this section, the explicit total Lagrangian FPM was employed to solve several validation case studies encompassing both 2D and 3D domains. The proposed method was evaluated in simulations of finite deformation at different levels of extension and compression. In all cases, hyperelastic material behaviour was considered using the standard neo-Hookean constitutive model with near-incompressibility. The strain energy density of this model was given in terms of the reduced invariants by:

$$W(J_1, J_3) = \frac{\mu}{2}(J_1 - 3) + \frac{K}{2}(J_3 - 1)^2 \tag{27}$$

where μ is the material's shear modulus, K denotes its bulk modulus, and J_1, J_3 denote the first and third reduced invariants. The solutions obtained from FPM were compared with solutions obtained from FEM using nodally-integrated simplicial elements to avoid volumetric locking [33]. To ensure a one-to-one comparison, the nodes of the FEM meshes were used for the FPM discretization. The discretization subdomains were generated using a dual polyhedral mesh generation algorithm [34, 35]. Comparison was performed measuring the normalized root mean square error ($NRMSE$) of the obtained displacements from both FPM and FEM, which is given by:

$$\text{NRMSE} = \frac{\sqrt{\dfrac{\sum_{j=1}^{n} \left(u_j^h - u_j^{ref}\right)^2}{n}}}{\max_j u_j^{ref} - \min_j u_j^{ref}} \tag{28}$$

where u^h denotes the numerical solution obtained either by FPM or FEM, u^{ref} the reference solution, and n the number of nodes of the discretization. All simulations were performed on a laptop with Intel® Core™ i9-12900H CPU and 32GB RAM.

3.1 Penalty coefficient effect on interior penalty numerical flux correction

In this case study, the effect of the penalty coefficient (p) on the interior penalty numerical flux correction was evaluated. Two simulation scenarios of a 2D neo-Hookean material with dimensions 10×4 m (nodes: 125) undergoing 20% extension and 20% compression were considered. Material density $(\rho) = 1000$ kg/m^3, Young's modulus (YM) $= 3$ kPa, and Poisson's ratio $(\nu) = 0.45$ were set. The material was constrained at $x = 0$ m applying zero displacement conditions $u_x = 0$ m, $u_y = 0$ m. At $x = 10$ m, the displacement condition $u_x = 2$ m was applied for the case of constrained extension, while $u_x = -2$ m was applied for constrained compression. Simulations were performed using $p = \{0, 10, 20, 50, 100\}$, where the obtained solution for $p = 100$ was considered as the reference solution. When $p = 0$, the solution was discontinuous at the subdomain interfaces, leading to the inconsistency problem observed in Figure 2.

By increasing p, the discontinuity of the solution between the subdomains was reduced. For $p > 0$, the consistency and accuracy were restored as shown in Figure 3. From the NRMSE evaluation of the solutions with $p = 0 - 50$ compared to the solution with $p = 100$, accurate results were obtained for $p \geq 20$. For the case of constrained extension, NRMSE was found in the range $[6.48\text{e}{-5}, 1.54\text{e}{-2}]$, while for constrained compression, the NRMSE was found in the range $[5.32\text{e}{-5}, 7.01\text{e}{-2}]$. Recall from Equation (26) that as p increases, the critical stable time step is reduced by $\sqrt{p}$. In order to ensure good accuracy and efficiency in the following examples, simulations were performed using $p = 20$ as it was found to be a good trade-off value between accuracy and computational efficiency.

3.2 Unconstrained compression of a 3D hyperelastic block

In this case study, the unconstrained compression problem was solved for a 3D hyperelastic block with dimensions $0.1 \times 0.1 \times 0.1$ m^3. Unconstrained compression was simulated applying the following boundary conditions. $u_x = 0$ m at $x = 0$ m, $u_y = 0$ m at $y = 0$ m, $u_z = 0$ m at $z = 0$ m, and $u_z = 0.04$ m at $z = 0.1$ m. The block was modelled as a neo-Hookean material with $\rho = 1000$ kg/m^3, YM $= 3$ kPa, and $\nu = 0.45$. The problem was

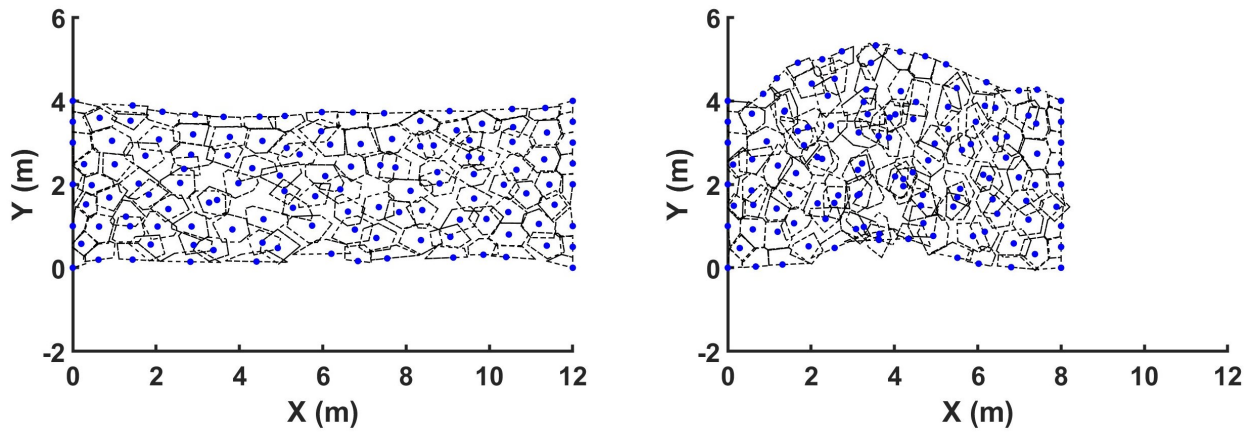

(a) 20% extension (b) 20% compression

Figure 2: Deformation of a 2D hyperelastic material using the explicit total Lagrangian Fragile Points Method (FPM) without interior penalty numerical flux correction ($p = 0$). The inconsistency of the solution is evident due to the discontinuity of the FPM trial and test functions.

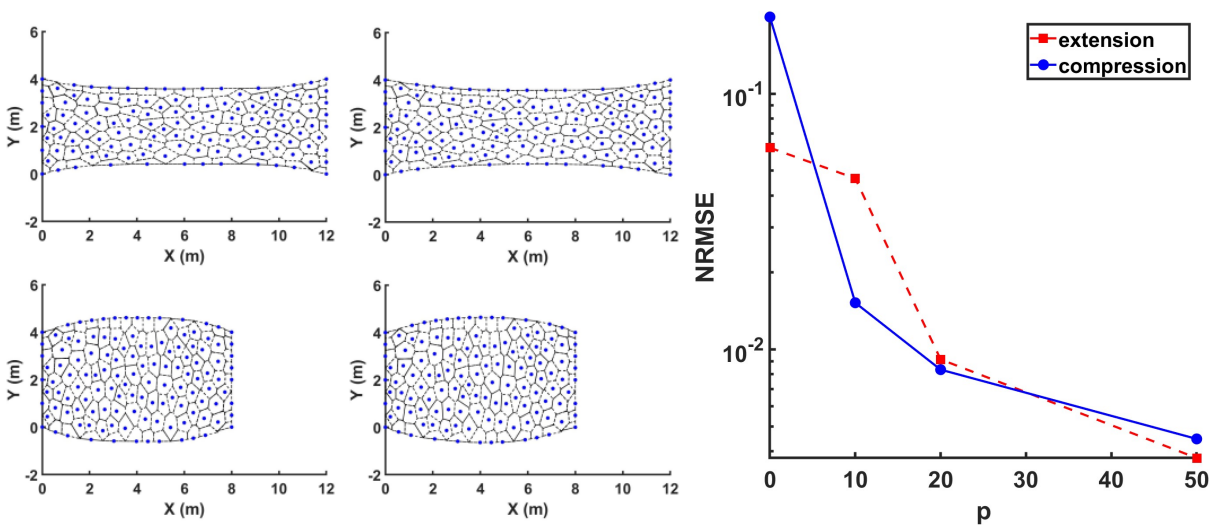

(a) $p = 20$ (b) $p = 100$ (c)

Figure 3: Deformation of a 2D hyperelastic material at 20% extension (top) and 20% compression (bottom) using the explicit total Lagrangian FPM with interior penalty numerical flux correction with penalty coefficient (a) $p = 20$ and (b) $p = 100$. (c) $NRMSE$ for solutions with $p = 0 - 50$ compared to a solution with $p = 100$ for 20% extension (red square) and 20% compression (blue bullet).

solved using FPM with $p = 20$ and FEM for four different mesh resolutions with h = 1.09e-2 – 3.73e-3, where h was the average nodal spacing (see Table 1). The NRMSE of the displacement was evaluated for both FPM and FEM solutions compared to the reference analytical solution $u_{ref} = -0.4z$, where z denotes the Z-component of the nodes coordinates at the reference configuration. A qualitative comparison as well as the NRMSE convergence plots for FPM and FEM solutions are provided in Figure 4. The NRMSE for the different mesh resolution levels and the execution time for the computation of the FPM (t_{FPM}) and FEM (t_{FEM}) solutions are reported in Table 1. The execution time was normalized with respect to the execution time of the FEM solution for mesh resolution with $h = 1.09e - 2$ m ($t_{FEM} = 2.84$ s).

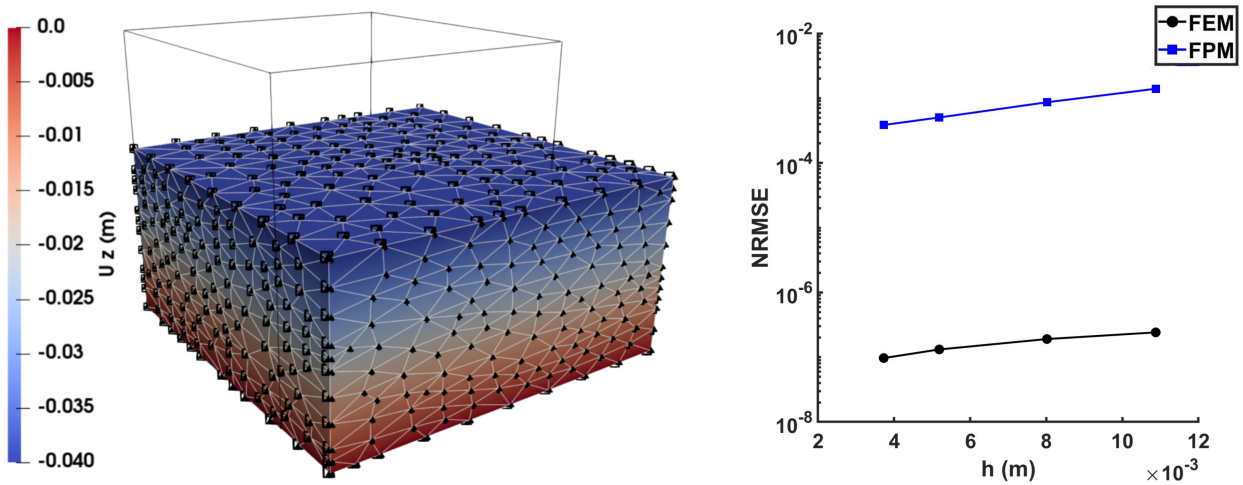

(a) (b)

Figure 4: (a) 40% unconstrained compression of a 3D hyperelastic material using FPM (triangle) and FEM (square) for mesh with h = 1.09e-2 m. (b) $NRMSE$ of the displacement (u_z) obtained by FEM (black bullet) and FPM (blue square) for meshes with h = 1.09e-2 – 3.73e-3 m compared to the analytical solution $u_z = -0.4z$, where z denotes the z coordinate of the mesh nodes at the reference configuration.

Table 1: $NRMSE$ and execution time report for Fragile Points Method (FPM) and Finite Element Method (FEM) solutions for the unconstrained compression of a 3D hyperelastic block.

Nodes	**h (m)**	**NRMSE**$_{FPM}$	**t**$_{FPM}$	**NRMSE**$_{FEM}$	**t**$_{FEM}$
1639	1.09e-2	13.979e-4	1.39	2.416e-7	1
3843	8.02e-3	8.650e-4	3.81	1.907e-7	1.92
13144	5.19e-3	5.036e-4	19.93	1.317e-7	10.17
34064	3.73e-3	3.855e-4	83.2	0.969e-7	37.62

FPM execution time (t$_{FPM}$) and FEM execution time (t$_{FEM}$) were normalized with respect to t$_{FEM}$ $= 2.84$ s, obtained from the FEM solution of the mesh resolution with h = 1.09e-2 m

3.3 Constrained extension of a 3D hyperelastic block

In this case study, the constrained extension of the 3D neo-Hookean block in Example 3.2 was considered. Zero displacement boundary conditions, $u_x = 0$ m, $u_y = 0$ m, $u_z = 0$ m, were applied at $z = 0$ m to fully constrain the bottom surface of the block. The top surface was constrained at $X-$ and $Y-$ directions applying $u_x = 0$ m and $u_y = 0$ m at $z = 0.1$ m. A fixed displacement $u_z = g$, where $g = 0.06, 0.1, 0.2$ m was applied at $z = 0.1$ m to simulate the extension of the block by 60%, 100%, and 200% of its initial height, respectively. FPM solutions were obtained using $p = 20$ and compared to solutions obtained from FEM for all the mesh refinement levels. Since an analytical solution was not available for this problem, the NRMSE for both FPM and FEM solutions was computed compared to a reference solution for a dense mesh with 80220 nodes and h = 2.79e-3 m. Prior to the NRMSE calculation, the FPM and FEM solutions for all the mesh refinement levels were mapped to the dense reference mesh using the Moving Least Squares approximation [36]. The NRMSE convergence plots are provided in Figure 5.

From the obtained NRMSE values for the different mesh refinement levels (see Table 2), the NRMSE convergence of FPM solution was in closer agreement with FEM compared to Example 3.2. This was mainly due to the increased mesh distortion in this example leading to numerical accuracy deterioration in the FEM solution. The mesh distortion effect in FEM accuracy was more evident in the case of the 200% extension where the error was two orders of magnitude higher than the error in the 60% and 100% extensions. It should be noted that this accuracy deterioration was not observed in FPM where the error was maintained at the same order for all the extension cases.

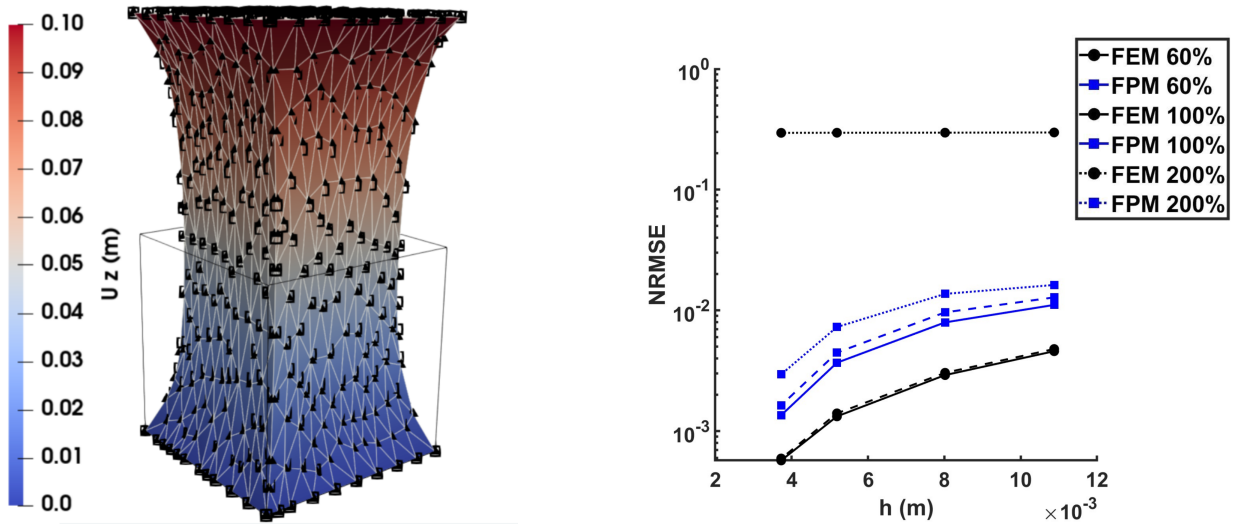

(a) (b)

Figure 5: (a) 100% constrained extension of a 3D hyperelastic material using FPM (triangle) and FEM (square) for mesh with h = 1.09e-2 m. (b) $NRMSE$ of the displacement field ($\boldsymbol{u}$) obtained by FEM (black bullet) and FPM (blue square) for meshes with h = 1.09e-2 – 3.73e-3 m compared to the solution for the reference mesh with h = 2.79e-3 m at 60%, 100%, and 200% extension of the block's initial height.

Table 2: $NRMSE$ report for FPM and FEM solutions for the constrained extension of a 3D hyperelastic block at 60%, 100%, and 200% of its initial height.

h (m)	**NRMSE**$_{FPM}$			**NRMSE**$_{FEM}$		
	60%	100%	200%	60%	100%	200%
1.09e-2	1.110e-2	1.282e-2	1.625e-2	4.592e-3	4.788e-3	2.978e-1
8.02e-3	7.956e-3	9.633e-3	1.370e-2	2.912e-3	3.043e-3	2.967e-1
5.19e-3	3.688e-3	4.469e-3	7.282e-3	1.325e-3	1.403e-3	2.963e-1
3.73e-3	1.354e-3	1.636e-3	2.954e-3	5.716e-4	5.935e-4	2.957e-1

3.4 Constrained compression of a 3D hyperelastic block

In this case study, the setup of Example 3.3 was used to simulate constrained compression of 20%, 40%, and 60% of the initial height by applying the fixed displacement boundary condition $u_z = -l$, where $l = 0.02, 0.04, 0.06$ m and $z = 0.1$ m at the top surface. The same material properties and zero displacement boundary conditions as in Example 3.3 were applied in this scenario. Similarly, NRMSE was computed for FPM and FEM solutions; convergence plots are provided in Figure 6.

NRMSE values for FPM and FEM solutions of the constrained compression problem are given in Table 3. It is shown that the error has the same order of magnitude for FPM and FEM solutions for the cases of 20% and 40%. However, as can be seen in Figure 6a, the FEM solution at 40% compression leads to highly distorted elements, especially at the corners of the geometry (square markers out of the deformed geometry). For 60% compression, FPM converges in a smooth deformation state. However, NRMSE increases by one order of magnitude compared to the 20% and 40% compression cases. However, it should be noted that FEM solutions could not be obtained for 60% since FEM could not converge for a compression rate higher than 40%.

4 Discussion

Meshless methods have demonstrated their suitability compared to FEM for the large deformation of hyperelastic materials since the latter suffers from accuracy deterioration due to mesh distortion [2, 3]. However, common meshless

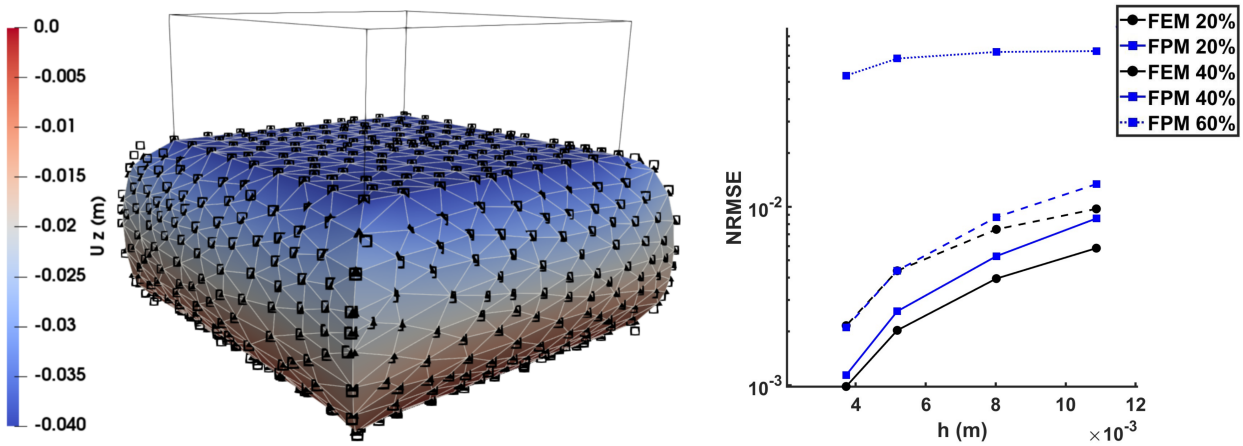

(a) (b)

Figure 6: (a) 40% constrained compression of a 3D hyperelastic material using FPM (triangle) and FEM (square) for mesh with h = 1.09e-2 m. (b) $NRMSE$ of the displacement field ($\boldsymbol{u}$) obtained by FEM (black bullet) and FPM (blue square) for meshes with h = 1.09e-2 – 3.73e-3 m compared to the solution for the reference mesh with h = 2.79e-3 m at 20%, 40%, and 60% compression of the block's initial height. Note that FEM is unable to converge for compression larger than 40%.

Table 3: $NRMSE$ report for FPM and FEM solutions for the constrained compression of a 3D hyperelastic block at 20%, 40%, and 60% of its initial height. Note that FEM failed to converge for 60% constrained compression.

h (m)	**NRMSE**$_{FPM}$			**NRMSE**$_{FEM}$		
	20%	40%	60%	20%	40%	60%
1.09e-2	8.590e-3	1.338e-2	7.445e-2	5.856e-3	9.723e-3	-
8.02e-3	5.281e-3	8.741e-3	7.363e-2	3.955e-3	7.464e-3	-
5.19e-3	2.594e-3	4.385e-3	6.764e-2	2.029e-3	4.377e-3	-
3.73e-3	1.139e-3	2.102e-3	5.423e-2	9.832e-4	2.155e-3	-

methods are usually more computationally expensive than FEM and require additional treatment for the exact imposition of boundary conditions. In this work, the Fragile Points Method (FPM) was considered for large deformation simulations as it delivers the advantages of meshless methods while overcoming their limitations. FPM is a novel meshless method which employs simple polynomials, which are local and discontinuous, as trial and test functions. Compared to other meshless methods, it has the advantage of simple and exact imposition of boundary conditions as in FEM. Moreover, the approximation is performed on compact support domains with simple trial and test functions that allow for accurate results with low-order integration. Therefore, the computational overhead of other meshless methods is significantly reduced for FPM. However, due to the discontinuity of trial and test functions in FPM, it is necessary to apply an interior penalty numerical flux correction to obtain consistent and accurate results. Since explicit time integration was used for the formulation of the total Lagrangian algorithm, the critical stable time step had to be reduced by the square root of the penalty coefficient (p) to ensure stability. Therefore, the value of p should be chosen carefully to obtain accurate results without significantly reducing efficiency. In Example 3.1, different values of $p = 0 - 100$ were investigated and $p = 20$ was found to be a good trade-off value between accuracy and efficiency.

The computational time of FPM compared to FEM was evaluated in Example 3.2. It was found that $t_{FPM} = \gamma t_{FEM}$, with $\gamma \in [1.39, 2.2]$ being the FPM computational overhead which was mainly due to the evaluation of the first Piola–Kirchhoff stress tensor twice at each interface ($\boldsymbol{P}^+$, $\boldsymbol{P}^-$) during the computation of the interior penalty numerical flux correction at each integration time step. It should be noted that FPM execution time was compared with FEM execution time for FEM simulations employing simplicial elements. It is expected that if higher order elements were to be used, the FPM computational overhead should be lower compared to FEM. Therefore, it can be claimed that FPM is an efficient meshless method for large deformation simulation of hyperelastic materials.

In terms of accuracy, the performed experiments verified our initial hypothesis that FPM is a promising alternative to FEM when large mesh distortion occurs during deformation. Computing the normalized root mean square error,

it was observed in case study 3.2 that FEM had superior convergence compared to FPM for the simple case of the unconstrained compression of a hyperelastic block. This was expected as the mesh distortion was not severe in this case. However, when cases with higher mesh distortion were considered, e.g. case studies 3.3 and 3.4, the NRMSE convergence of FEM was significantly reduced by four orders of magnitude. In contrast, the same order of magnitude was maintained for FPM convergence in all case studies. Most importantly, the FPM convergence was maintained even for the extreme cases of 200% extension and 60% compression of the initial height of the hyperelastic block. However, FEM convergence was not deteriorated for the case of 200% extension. Furthermore, at 60% compression a solution by FEM was not available since FEM failed to converge for compression rates larger than 40%.

The simple neo-Hookean constitutive model was used in each case study despite it not being suitable for very large deformations. Nevertheless, FPM was able to produce smooth solutions even for the extreme deformation cases at 200% extension and 60% compression. The obtained results from this study demonstrated the capacity of the FPM implementation of the explicit total Lagrangian algorithm to simulate large deformations even for cases where large mesh distortion was involved and FEM failed to provide an accurate solution.

5 Conclusion

In this work, the Fragile Points Method (FPM) was employed to derive the explicit total Lagrangian algorithm and simulate the deformation of hyperelastic materials undergoing large deformation. Validation case studies were performed to evaluate the method against the standard Finite Elements Method (FEM). The results revealed that when mesh distortion is involved, FEM accuracy is deteriorated as expected, but FPM retains its accuracy. Moreover, FPM has minimal computational overhead and it leads to smooth solutions even for extreme deformation scenarios where FEM fails to converge. Therefore, we can conclude that FPM is a suitable meshless alternative to FEM for finite deformation of hyperelastic materials, especially for the simulation of severe deformation.

In future work, the proposed algorithm will be used to simulate soft tissue deformation during cardiac surgery procedures (e.g., catheter ablation) and cardiac electromechanics. It is also expected the proposed algorithm will be evaluated with more sophisticated constitutive materials such as the Holzapfel-Gasser-Ogden [37] and Guccione [38] constitutive models. In the context of soft tissue simulation where time restrictions of the corresponding clinical application may apply, the work presented in [39] is of great interest. The use of neural networks as function approximators was proposed to accelerate the explicit total Lagrangian algorithm by allowing the use of a time step up to 20 times larger than the critical stable time step. It is expected that by using the explicit total Lagrangian FPM for training data generation, the neural network could generate accurate results for a wide range of deformations.

Acknowledgements

This work has received funding from the European Union's Horizon 2020 research and innovation programme under the Marie Skłodowska-Curie grant agreement PhyNeTouch No 101024463.

Conflict of interest

The authors declare no potential conflict of interests.

References

[1] OH Yeoh. Hyperelastic material models for finite element analysis of rubber. *Journal of Natural Rubber Research*, 12:142–153, 1997.

[2] De'an Hu and Zhanhua Sun. The meshless local petrov–galerkin method for large deformation analysis of hyperelastic materials. *International Scholarly Research Notices*, 2011, 2011.

[3] David S Malkus and Thomas JR Hughes. Mixed finite element methods–reduced and selective integration techniques: a unification of concepts. *Computer Methods in Applied Mechanics and Engineering*, 15(1):63–81, 1978.

[4] LDC Ramalho, J Belinha, and RDSG Campilho. A novel robust remeshing finite element technique for fracture propagation. *International Journal of Computational Methods*, 18(02):2050040, 2021.

[5] Joe J Monaghan. Smoothed particle hydrodynamics. *Reports on progress in physics*, 68(8):1703, 2005.

[6] Kenny WQ Low, Chun Hean Lee, Antonio J Gil, Jibran Haider, and Javier Bonet. A parameter-free total lagrangian smooth particle hydrodynamics algorithm applied to problems with free surfaces. *Computational Particle Mechanics*, 8(4):859–892, 2021.

[7] Satya N Atluri and Tulong Zhu. A new meshless local petrov–galerkin (mlpg) approach in computational mechanics. *Computational Mechanics*, 22(2):117–127, 1998.

[8] DA Hu, SY Long, X Han, and GY Li. A meshless local petrov–galerkin method for large deformation contact analysis of elastomers. *Engineering Analysis with Boundary Elements*, 31(7):657–666, 2007.

[9] Ted Belytschko, Yun Yun Lu, and Lei Gu. Element-free galerkin methods. *International Journal for Numerical Methods in Engineering*, 37(2):229–256, 1994.

[10] Qiang Wu, PiaoPiao Peng, and YuMin Cheng. The interpolating element-free galerkin method for elastic large deformation problems. *Science China Technological Sciences*, 64(2):364–374, 2021.

[11] Èric Lluch, Mathieu De Craene, Bart Bijnens, Maxime Sermesant, Jérôme Noailly, Oscar Camara, and Hernán G Morales. Breaking the state of the heart: meshless model for cardiac mechanics. *Biomechanics and Modeling in Mechanobiology*, 18(6):1549–1561, 2019.

[12] JK Chen, JE Beraun, and TC Carney. A corrective smoothed particle method for boundary value problems in heat conduction. *International Journal for Numerical Methods in Engineering*, 46(2):231–252, 1999.

[13] Grand Roman Joldes, Habib Chowdhury, Adam Wittek, and Karol Miller. A new method for essential boundary conditions imposition in explicit meshless methods. *Engineering Analysis with Boundary Elements*, 80:94–104, 2017.

[14] Grand Joldes, George Bourantas, Benjamin Zwick, Habib Chowdhury, Adam Wittek, Sudip Agrawal, Konstantinos Mountris, Damon Hyde, Simon K Warfield, and Karol Miller. Suite of meshless algorithms for accurate computation of soft tissue deformation for surgical simulation. *Medical Image Analysis*, 56:152–171, 2019.

[15] Ashley Horton, Adam Wittek, Grand Roman Joldes, and Karol Miller. A meshless total lagrangian explicit dynamics algorithm for surgical simulation. *International Journal for Numerical Methods in Biomedical Engineering*, 26(8):977–998, 2010.

[16] Konstantinos A Mountris, George C Bourantas, Daniel Millán, Grand R Joldes, Karol Miller, Esther Pueyo, and Adam Wittek. Cell-based maximum entropy approximants for three-dimensional domains: Application in large strain elastodynamics using the meshless total lagrangian explicit dynamics method. *International Journal for Numerical Methods in Engineering*, 121(3):477–491, 2020.

[17] George Bourantas, Benjamin F Zwick, Grand R Joldes, Adam Wittek, and Karol Miller. Simple and robust element-free galerkin method with almost interpolating shape functions for finite deformation elasticity. *Applied mathematical modelling*, 96:284–303, 2021.

[18] Thomas Most and Christian Bucher. A moving least squares weighting function for the element-free galerkin method which almost fulfills essential boundary conditions. *Structural Engineering and Mechanics*, 21(3):315–332, 2005.

[19] Annamaria Mazzia, Massimiliano Ferronato, Giorgio Pini, and Giuseppe Gambolati. A comparison of numerical integration rules for the meshless local petrov–galerkin method. *Numerical Algorithms*, 45(1):61–74, 2007.

[20] Vinh Phu Nguyen, Timon Rabczuk, Stéphane Bordas, and Marc Duflot. Meshless methods: a review and computer implementation aspects. *Mathematics and computers in simulation*, 79(3):763–813, 2008.

[21] Leiting Dong, Tian Yang, Kailei Wang, and Satya N Atluri. A new fragile points method (fpm) in computational mechanics, based on the concepts of point stiffnesses and numerical flux corrections. *Engineering Analysis with Boundary Elements*, 107:124–133, 2019.

[22] Tian Yang, Leiting Dong, and Satya N Atluri. An elementarily simple galerkin meshless method: The fragile points method (fpm) using point stiffness matrices, for 2d elasticity problems in complex domains. *ArXiv*, abs/1909.04149, 2019.

[23] Tadeusz Liszka and Janusz Orkisz. The finite difference method at arbitrary irregular grids and its application in applied mechanics. *Computers & Structures*, 11(1-2):83–95, 1980.

[24] Douglas N Arnold, Franco Brezzi, Bernardo Cockburn, and L Donatella Marini. Unified analysis of discontinuous galerkin methods for elliptic problems. *SIAM journal on numerical analysis*, 39(5):1749–1779, 2002.

[25] Yue Guan, Rade Grujicic, Xuechuan Wang, Leiting Dong, and Satya N Atluri. A new meshless "fragile points method" and a local variational iteration method for general transient heat conduction in anisotropic nonhomogeneous media. part ii: Validation and discussion. *Numerical Heat Transfer, Part B: Fundamentals*, 78(2):86–109, 2020.

[26] Konstantinos A Mountris, Leiting Dong, Yue Guan, Satya N Atluri, and Esther Pueyo. Meshfree implementation of the cardiac monodomain model through the fragile points method. *methods*, 11:12, 2021.

[27] Konstantinos A Mountris and Esther Pueyo. A meshless fragile points method for rule-based definition of myocardial fiber orientation. *SSRN*, 4073648, 2022.

[28] Yue Guan, Leiting Dong, and Satya N Atluri. A new meshless fragile points method (fpm) with minimum unknowns at each point, for flexoelectric analysis under two theories with crack propagation, i: Theory and implementation. *Journal of Mechanics of Materials and Structures*, 16(2):159–195, 2021.

[29] Kailei Wang, Baoying Shen, Mingjing Li, Leiting Dong, and Satya N Atluri. A fragile points method, with an interface debonding model, to simulate damage and fracture of u-notched structures. *International Journal for Numerical Methods in Engineering*, 123(8):1736–1759, 2022.

[30] Jerrold E Marsden and Thomas JR Hughes. *Mathematical foundations of elasticity*. Courier Corporation, 1994.

[31] Grand Roman Joldes, Adam Wittek, and Karol Miller. Stable time step estimates for mesh-free particle methods. *International Journal for Numerical Methods in Engineering*, 91(4):450–456, 2012.

[32] Ludovic Noels and Raúl Radovitzky. An explicit discontinuous galerkin method for non-linear solid dynamics: Formulation, parallel implementation and scalability properties. *International Journal for Numerical Methods in Engineering*, 74(9):1393–1420, 2008.

[33] MW Gee, CR Dohrmann, SW Key, and WA2512962 Wall. A uniform nodal strain tetrahedron with isochoric stabilization. *International Journal for Numerical Methods in Engineering*, 78(4):429–443, 2009.

[34] Rao V Garimella, Jibum Kim, and Markus Berndt. Polyhedral mesh generation and optimization for non-manifold domains. In *Proceedings of the 22nd International Meshing Roundtable*, pages 313–330. Springer, 2014.

[35] Jibum Kim. An efficient approach for solving mesh optimization problems using newton's method. *Mathematical Problems in Engineering*, 2014, 2014.

[36] Peter Lancaster and Kes Salkauskas. Surfaces generated by moving least squares methods. *Mathematics of computation*, 37(155):141–158, 1981.

[37] Gerhard A Holzapfel, Thomas C Gasser, and Ray W Ogden. A new constitutive framework for arterial wall mechanics and a comparative study of material models. *Journal of elasticity and the physical science of solids*, 61(1):1–48, 2000.

[38] Julius M Guccione, Andrew D McCulloch, and LK Waldman. Passive material properties of intact ventricular myocardium determined from a cylindrical model. *Journal of Biomechanical Engineering*, 113(1):42–55, 1991.

[39] Felix Meister, Tiziano Passerini, Viorel Mihalef, Ahmet Tuysuzoglu, Andreas Maier, and Tommaso Mansi. Deep learning acceleration of total lagrangian explicit dynamics for soft tissue mechanics. *Computer Methods in Applied Mechanics and Engineering*, 358:112628, 2020.